NEAR WAKE STRUCTURE OF FINITE CYLINDERS IN AN OPEN CHANNEL FLOWS

S. S. Paul
Department of Mechanical & Manufacturing Engineering
University of Manitoba, Winnipeg, MB
R3T 5V6
sspaul04@yahoo.ca

M. F. Tachie
Department of Mechanical & Manufacturing Engineering
University of Manitoba, Winnipeg, MB
R3T 5V6
tachiemf@cc.umanitoba.ca

ABSTRACT

The paper reports on an experimental study of turbulent flow in the near-wake region of four different finite cylinders. A particle image velocimetry technique was used to conduct detailed velocity measurements around and in the near-wake of the cylinder models. The contours as well as profiles of the mean velocities and turbulence intensities were obtained to document the salient features of the flow field. The proper orthogonal decomposition and two-point correlation functions were then applied to provide an insight into the structure of the flow. Reconstruction of the fluctuating velocity components for various numbers of POD modes were also used to investigate the role of large-scale structures.

INTRODUCTION

Turbulent flows around bluff bodies have received considerable research attention due to their practical importance in a wide range of environmental and fluid engineering applications. These include flow past high-rise buildings, overhead cables and hydraulic structures such as bridge piers. The two-dimensional turbulent wakes generated by an infinite circular and square cylinder in a uniform flow are the prototypical configurations that have been studied most extensively. Excellent review and discussions on turbulent wakes in uniform flows have been presented, for example, by Zdravkovich (2003)

Although the fluid flow around the infinite cylinder is now reasonably well understood, detailed quantitative experimental information in the near wake region of a finite cylinder of various cross-sections is limited. It should be remarked that the finite length of the cylinder pertains to the non-negligible end effects that invariably enhance 3-*D* flow characteristics over all Reynolds number ranges (Park and Lee, 2002). One of the salient features of flow over a 3-*D* bluff body is flow separation from the top and side surfaces. The separated flow is shed periodically downstream. Near the ground surface, one or more vortices are induced and stretched into the shape of a horseshoe (Park and Lee, 2002). Okamato and Sunabashiri (1992) and Park and Lee (2004) found that the free-end downwash shear layer plays an important role in the formation of the near wake. For an aspect ratio in the range of 3 to 4, the free-end shear layer attaches on the wall. Extensive reviews and discussion can be found in Sumner *et al.* (2004) and Adaramola et al. (2007). In spite of the previous investigations, only a few studies have measured the wake velocity field of a finite cylinder (Adaramola *et al.* 2007).

The objective of the present study is to investigate the effects of cylinders cross-section (circular, square, and trapezoidal-shaped) on the mean velocity and turbulence statistics in the near wake region of finite cylinders. Subsequently, the flow structure is studied in detail using the proper orthogonal decomposition (POD) and two-point correlation functions.

EXPERIMENTAL METHOD

The schematic of a three-dimensional view of the inserted test section with the cylinder, the CCD camera, and the laser arrangements are shown in Figure 1a. Figure1b shows the plan view of the cylinder models: b (*i*), b (*ii*), b (*iii*), and b (*iv*), show, respectively, the circular (CC), square (SQ), trapezoidal-shape with the longer side (S_{z1}) facing the oncoming flow (DS), and trapezoidal-shape with the shorter side (S_{z2}) facing the oncoming flow (DR). It should be remarked that Figure 1b (iii) is a mirror image of 1b (iv) and that the radius, R = 12.7 mm.

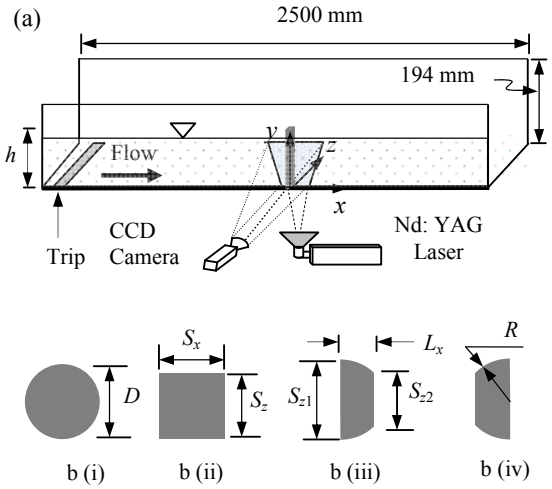

Figure 1: (a) A 3-D view of test section, the CCD camera, and the laser arrangements with the coordinate system, (b) plan view of cylinder models: b(i) Circular (CC), b(ii) Square (SQ), b(iii) & b(iv) Trapezoidal-shaped, respectively, DS and DR.

As shown, x, y, and z are, respectively, in the streamwise, transverse and spanwise directions; x = 0 is at the trailing edge of the cylinder which is located at 1250 mm from the inlet of the test section, y = 0 is at the floor of the inserted test section, and z = 0 is at the channel mid-span.

The approach free stream velocity close to the free surface (U_e = 0.26 m/s) and the water depth, h (= 75 ± 2 mm) were kept constant in all the experiments. The wake measurements were performed in the x-z plane at mid-depth of flow (i.e., at h = 37.5 ± 1 mm). The Reynolds number based on depth of flow and boundary layer momentum thickness, were, respectively, 19500 and 1540. Prior to conducting measurements around the cylinder in the x-z plane, the approach flow was characterized upstream of the leading edge of the cylinder at $x/D \approx -20$ in the x-y plane located at mid-span of the channel. The boundary layer thickness defined as the y-location where $U = 0.99U_e$ was 63 mm. This implies that the mid-depth where the wake measurements were conducted is within the boundary layer.

A PIV technique was used to conduct the velocity measurements. The flow was seeded with 5 μm polyamide seeding particles having a specific gravity of 1.03. An Nd-YAG, 120 mJ/pulse laser of 532 nm wavelength was used to illuminate the flow field. The laser sheet was located at the mid-plane of the channel and perpendicular to the camera. A 12-bit high-resolution digital camera (Dantec Dynamic HiSense 4M camera) that uses a CCD with 2048 pixels × 2048 pixels and has a 7.4 μm pixel pitch was used to image the flow field. The measurements were made at a field of view of 105 mm × 105 mm which corresponds to 8.3D × 8.3D in the streamwise and spanwise directions of the flow. The instantaneous images were processed using the adaptive correlation option of FlowManager developed by Dantec Dynamics Inc. A three-point Gaussian curve fit was used to determine particle displacement with sub-pixel accuracy. An interrogation area of 32 pixels × 32 pixels with 50% overlap was employed. With this interrogation area size, the spacing between adjacent vectors is 0.82 mm or 0.06D. The particle image diameter was d_p = 2.1 pixels, which is very close to the recommended optimum value of $d_p \approx 2$ pixels required to minimize peak locking (Raffel et al 1998). Based on preliminary convergence tests, 2000 instantaneous image pairs were used to compute the mean velocity and turbulence statistics reported subsequently.

Measurement uncertainty analysis was made following the AIAA standard derived and explained by Coleman and Steele (1995). The guidelines and steps necessary to minimize the bias and precision errors in PIV measurements are discussed by Prasad et al (1992) and Forliti et al (2000). In this study, the uncertainties in the mean velocities and turbulence intensities at 95% confidence level were estimated to be ±2% and ±6%, respectively, of the corresponding maximum values.

RESULTS AND DISCUSSION

Contours of Mean Velocity

The contour plots of the normalized mean streamwise velocity, (U/U_{max}) obtained at mid-depth of flow are shown in Figure 2 to reveal some qualitative features of the flow pattern around the various cylinder models. The corresponding streamlines are superimposed to facilitate the interpretation of the results. The approximate locations of the cylinders are also shown in each figure. The U_{max} values used to normalize the data in Figures 4 and 5 are summarized in Table 1. These values were obtained at x/D = 2.5 downstream of the cylinders, and outside the wake region; i.e., where U is uniform or independent of z. As expected a pair of counter rotating vortices, nearly identical in size, is formed downstream of the cylinder. The topologies of the streamwise mean velocity revealed that blockage produced by the cylinders produced high velocity regions on either side of the cylinders, and extending to the outer edges of counter rotating vortices. As a result of entrainment of the ambient fluid into the wake region, the mean velocity across the wake decreases with downstream distance. The streamline topologies demonstrate some important differences in the flow patterns that can be attributed to the specific geometry of the cylinders. For example, the wake region behind the cylinders with sharp upstream edges (Tests SQ and DS) is relatively wider but shorter than those downstream of models with more rounded upstream edges (Tests CC and DR). From the streamline topologies, the spanwise width of the wake, W_f, is defined as the cross-stream distance between the separating shear layers on opposite sides of the wake axis passing through the foci. The axial locations, x_f/D, of the foci are presented in Table 1.

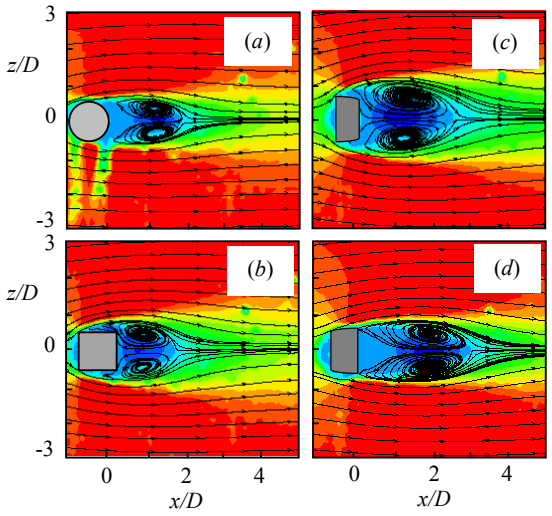

Figure 2: Contours of mean velocity (U/U_e): (a) CC; (b) SQ; (c) DS; and (d) DR.

The value of x_f/D = 1.5 for Tests DS and SQ is distinctly smaller than $x_f/D \approx 1.9$ and 2.2 for the cylinders with more rounded edges (Tests CC and DR, respectively). On the contrary, Table 1 demonstrates that the values of the non-dimensional spanwise width for cylinder models with sharp leading edges (Tests DS and SQ) are relatively larger than those with rounded leading edge (Tests DR and CC).

Table 1. Summary of test conditions and pertinent parameters.

Test	D (m/s)	U_{max} (m/s)	x_f/D	W_f/D	L_r/D	L_f/D
CC	12.2	0.282	1.9	1.3	2.6	2.8
SQ	12.8	0.284	1.5	1.6	2.3	2.5
DR	15.2	0.296	1.5	1.7	2.6	2.6
DS	15.2	0.298	2.2	1.3	3.1	3.1

The value of W_f/D = 1.15 for Test CC is relatively larger than the corresponding value of 0.95 reported by Ozgoren (2006). For the square cylinder (Test SQ), the present value of 1.56 is not significantly different from 1.48 obtained by Ozgoren (2006).

Profiles along the Wake

Figure 3a shows the distributions of the normalized mean streamwise velocity along the wake axis for the cylinder models. The streamwise mean velocity along the wake axis provides information about the length of the recirculation, L_r (which is defined as the distance between the center of the cylinder and the downstream location where the streamwise mean velocity becomes zero) as well as recovery of the mean flow towards the approach flow (*i.e.* U/U_{max} = 1). The values of L_r/D for the cylinder models are shown in Table 1. Figure 3a also reveals that, for all test cases, the magnitude of U/U_{max} initially decreases with distance along the wake axis with $(U/U_{max})_{min}$ occurring at about the middle of L_r and then start to increase thereafter. The values of $(U/U_{max})_{min}$ are approximately -0.16, -0.17, -0.17, and -0.22, respectively, for Tests SQ, CC, DR and DS. The subsequent recovery of the mean flow in the very near-wake region is fastest for Test SQ and slowest for Test DR.

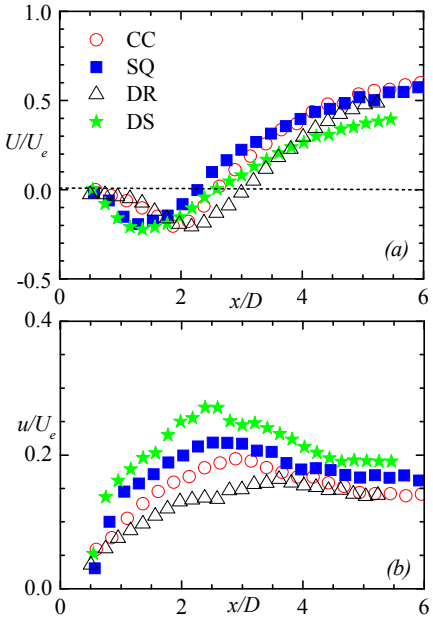

Figure 3: Mean velocities and turbulent quantities along the wake centerline: (a) streamwise mean velocity and (b) streamwise turbulent intensity.

The streamwise turbulence intensity (Figure 3b) increases along the wake axis to a maximum followed by a gradual decay. The vortex formation length, L_f, is defined as the downstream location of the cylinder where the streamwise velocity fluctuation level has increased to a maximum (Nakagawa *et al*., 1999). The values of $L_f/D \approx 2.8$ and 2.5 (Table 1) were obtained for Tests CC and SQ, respectively. The corresponding values for Tests DR and DS are, respectively, $L_f/D \approx 3.1$ and 2.6. It is clear from Table 1 that, for a given test condition, the location where U becomes zero (L_r) is not significantly different from the point where u_{max} occurred (L_f). The distributions of the turbulence intensity along the wake axis also depend on the specific geometry of the leading edge of the cylinder. More specifically, the profiles downstream of CC and DR are lower than observed for SQ and DS. It has been argued that, for a circular cylinder in a uniform flow, an increase in L_f/D is related to a decrease in turbulent intensity and the base suction (Williamson (1996).

Profiles across the Wake

The profiles of the normalized mean velocities and turbulence intensities across the wake at selected streamwise locations corresponding to the foci as well as x/D = 2.5, 5.0 and 10.0 are shown in Figures 4 and 5, respectively. The x-axis range of repeated section in Figure 4a is 0 to 2, while for Figure 4b it is 0 to 0.3. The x-axis range of repeated section in Figure 5 is 0 to 0.4. It is important to note that in these and subsequent plots, appropriate intermediate data points are skipped to avoid data congestion. These data sets, apart from providing additional insight into the downstream development of wake flow, would be useful for validating numerical results in the near-wake region of open channel flows. Figure 4a shows that the mean velocity, U/U_{max} at the axial location corresponding to the foci increase from negative values in the recirculation regions to maxima and then decrease to a value of unity. The profiles of U/U_{max} are symmetrical about the wake axis, z = 0. As the flow evolves downstream and entrains the ambient fluid, the wake spreads in the spanwise direction and the velocity deficit diminishes with x/D.

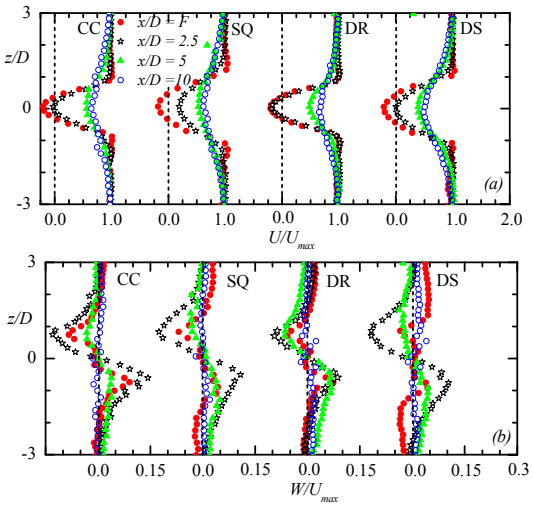

Figure 4: Mean velocities (a) U/U_{max} and (b) W/U_{max} at selected x/D locations across the wake.

The mean spanwise velocity, W/U_{max} profiles (Figure 4b) are anti-symmetric about the wake axis; that is, the values of W/U_{max} are predominantly positive for $z > 0$ and negative for $z < 0$. The spanwise mean velocity is as high as 16% of U_{max}. These high values together with the steep gradients $\partial W/\partial z$ in the very near wake region imply that the dynamic importance of the spanwise mean velocity in momentum transport cannot be neglected. Moreover, the contributions of W and $\partial W/\partial z$ to the convective and production terms in the transport equations for the Reynolds shear stress and turbulent kinetic energy should be accounted for in order to correctly predict the flow characteristics in the

near-wake region. At larger downstream location ($x/D > 5$), W/U_{max} decays very rapidly and $\partial W/\partial z$ diminishes.

The streamwise turbulent intensity, u/U_{max} (Figure 5a) shows the expected double peaks confirming the existence of pairs of vortices observed in Figure 4a. The double peaks become broader and less distinct with downstream distance. Unlike the streamwise turbulent intensity profiles, a single peak is observed in w/U_{max} with a maximum occurring along the wake axis (Figure 5b). It is interesting to note that the u-values are generally smaller than those of the w-values at all locations, signifying a more intense spanwise mixing.

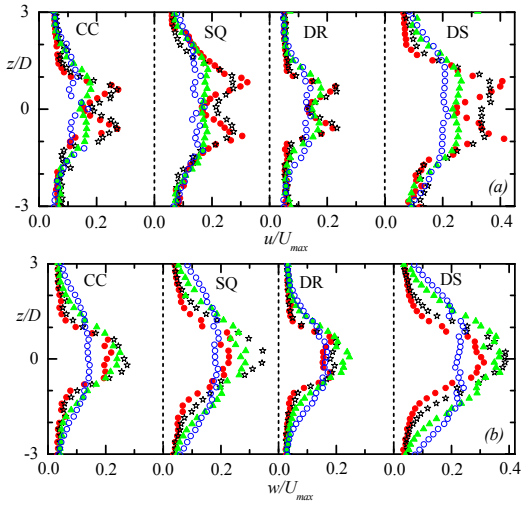

Figure 5: Variation of turbulence intensities (a) u/U_{max} and (b) w/U_{max} at selected x/D locations across the wake.

Although the trends in all test cases at the selected x/D locations appear to be qualitatively similar, a collapse of the profiles of *CC* and *DR* for $(U/U_e)_{\min}$ values and a similar collapse of the profiles of *SQ* and *DS* at a higher $(U/U_e)_{\min}$ values at the corresponding x/D locations (not shown) is observed in the wake region. For the turbulent quantities, however, *DS* consistently, reveals highest peak values closely followed by *SQ* with least values for *CC* and *DR*. These observations imply that the effect of leading edge geometry is more significant than that of the trailing edge.

POD ANALYSIS

Implementation

The POD analysis presented in this study follows the snapshot methodology proposed by Sirovich (1987). The specific implementation follows the procedure outlined by Meyer *et al*. (2007). By this method, each instantaneous PIV vector map is considered a snapshot of the flow, and the total number of vectors in each snapshot is designated by *M*, while the total number of snapshots is denoted by *N*. The snapshot method is computationally more efficient than the direct method when $M >> N$ as in the present PIV experiments. The streamwise (u) and transverse (v) components of the fluctuating velocity (u_j^n, w_j^n) are obtained by subtracting the ensemble averaged snapshot ($\overline{\boldsymbol{u}}$) from each snapshot ($\hat{\boldsymbol{u}}^n$), where the index n runs through the N snapshots and j runs through the M positions of velocity vectors in a given snapshot (*i.e.* $u_j = u(x_j, z_j)$). The fluctuating velocity components from the N snapshots are then arranged in a matrix $\boldsymbol{U}$ and the $N \times N$ auto-covariance matrix is obtained from

$$\boldsymbol{C} = \boldsymbol{U}^T\boldsymbol{U} \qquad (1)$$

A set of N eigenvalues, $\boldsymbol{\lambda}^i$, and a corresponding set of orthonormal eigenvectors, $\boldsymbol{A}^i$ which satisfy

$$\boldsymbol{C}\boldsymbol{A}^i = \boldsymbol{\lambda}^i\boldsymbol{A}^i \qquad (2)$$

can be evaluated from the auto-covariance matrix; where i runs from 1 to N. The eigenvalues are ordered by decreasing value as follows:

$$\boldsymbol{\lambda}^1 > \boldsymbol{\lambda}^2 > \ldots > \boldsymbol{\lambda}^N > 0 \qquad (3)$$

The normalized POD modes (ϕ^i) are constructed from the projection of the eigenvectors ($\boldsymbol{A}^i$) on to the original fields as follows:

$$\phi^i = \frac{\sum_{n=1}^{N} A_n^i u^n}{\left\| \sum_{n=1}^{N} A_n^i u^n \right\|}, \quad i = 1, \ldots, N. \qquad (4)$$

where $A_n{}^i$ is the nth component of the eigenvector corresponding to $\boldsymbol{\lambda}^i$. Here $\|.\|$ is the L_2-norm. The POD coefficients, a_i of each mode were calculated by projecting the fluctuating part of the velocity field onto the calculated POD modes as follows:

$$\boldsymbol{a}^n = \boldsymbol{\Psi}^T\boldsymbol{u}^n \qquad (5)$$

where, $\boldsymbol{\Psi} = [\boldsymbol{\phi}^1\ \boldsymbol{\phi}^2\ \ldots\ \boldsymbol{\phi}^N]$. The expansion of any member of the ensemble using an arbitrary number of modes m was performed using:

$$\tilde{u}^n = \sum_{i=1}^{m} a_i^n \phi^i = \psi a^n \qquad (6)$$

Equation 6 is known as the proper orthogonal decomposition of u^n; it gives the best approximation of the data ensemble u^n in the sense that the average least-squares truncation error is a minimum for any given number $m \leq N$ of basis functions over all possible sets of orthogonal basis functions.

The ensemble-averaged energy, E of the fluctuating component is given by the sum of all the eigenvalues (Equation 7) while the fractional contribution of each eigenfunction to the total energy is given by the fractional contribution of its associated eigenvalue (Equation 8).

$$E = \sum_{i=1}^{N} \lambda_i \qquad (7)$$

$$E_n / E = \lambda_n / \textstyle\sum_i^N \lambda_i \qquad (8)$$

RESULT AND POD APPLICATION

Convergence Test

Convergence of the POD analysis is defined as the ratio between the energy contained in the ith mode and the global energy contained within the flow (Patte-Rouland *et al*. 2001). It is noteworthy that the number of snapshots required to adequately capture the energy content for a given mode depends on the nature or complexity of the flow. To evaluate the sample size or snapshots necessary to obtain converged POD analysis in the present study, the fractional contributions of the first two eigenvalues ($\lambda_1{}^*$ and $\lambda_2{}^*$) with increasing number of snapshots were calculated (not shown). It is observed that, for $N \geq 400$, the variation of $\lambda_1{}^*$ and $\lambda_2{}^*$ with N are within ± 0.03 % except for Test *DS*. Even for Test DS, $\lambda_1{}^*$ = 23.1 ± 0.09 % and $\lambda_2{}^*$ = 21.0 ± 0.07 %. Based on these results, it was concluded that N =

2000 used in the present analysis is adequate to achieve converge results. The number of snapshots used in the present study is higher than $N = 500$ used to analyze the near-wake region of square cylinders with different inclinations to the approach flow (van Oudheusden *et al*. 2005) and rectangular cylinders with different aspect ratio (Shi *et al.* 2009).

The fractional and the cumulative contribution of the modes to the turbulent kinetic energy for all test cases are plotted in Figures 6a and 6b, respectively. The dominance of the first two modes in the POD analysis is evident in Figure 6a. The figure also reveals that the first two eigenvalues occur in pairs of almost equal values.

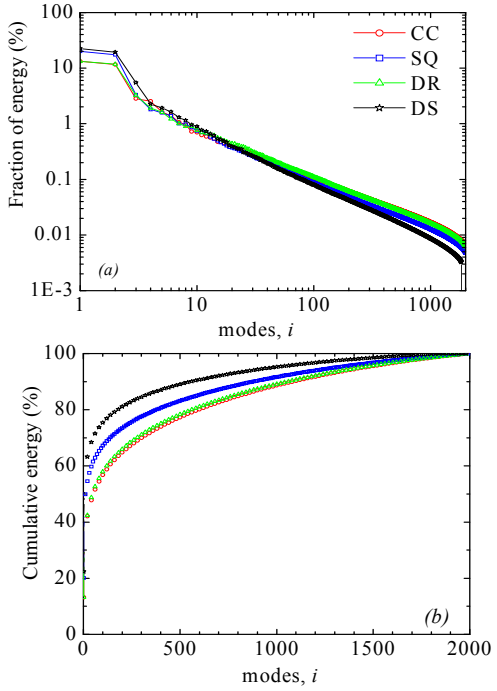

Figure 6: Spectra of turbulent kinetic energy for various test cases: (a) Fractional contribution to the turbulent kinetic energy by the modes, (b) Accumulated turbulent kinetic energy ratio of modes as a function of mode number.

As explained by Rempfer and Fasel (1994) this partnership indicates that the coherent structures of the flow are represented by spatio-temporal modes. This implies that the two spatial-modes linked to a pair of eigenvalues represent the same physical structure shifted only in the streamwise direction. Similar observations were made in the experimental study by van Oudheusden *et al*. (2005). The fractional contributions of the first two modes (λ_1^* and λ_2^*) to the total energy depend strongly on the geometry of the cylinder model. For example, $\lambda_1^* = 20\%$ and 22% for Tests SQ and DS, respectively. These values are approximately 54% to 70% higher than $\lambda_1^* = 13\%$ for the cylinders with rounded leading edge. These results imply that the large scale structures are more energetic downstream of cylinders with sharp leading edges compared to those found behind cylinders with more rounded leading edges. The energy associated with the modes decrease very rapidly with increasing mode for $i \geq 3$ (Figure 6a). For example, the fractional contribution to the total energy drops two orders of magnitude within the first 30 to 40 modes. The convergence of the cumulative contribution of POD modes towards 100% (Figure 6b) is relatively slow, as would be expected.

Eigenfunctions

The POD eigenfunctions represent the most common event occurring in the fluctuating field. Each mode represents a different flow structure embedded in the mean flow field. It also reveals different energy content in the velocity fluctuations. For example, the spatial flow structure characteristics exhibited by POD modes 1, 2, 3, and 5 for Test SQ are shown in Figure 7. Mode 1 displays two distinct vortical structures: counter-clockwise and clockwise centered respectively, at $x/D \approx 1$ and $x/D \approx 2.3$ (where stagnation point occurs in Figure 2) along the wake axis downstream of the cylinder. For the second mode, which roughly corresponds to the situation after half the shedding period of a single structure, the vortex position is displaced downstream. Mode 3 reveals a clockwise vortex structure whose centre is located at $y > 0$ and a counter-clockwise vortex structure whose centre is located at $y < 0$ with strong streamwise flows generated between the flapping vortices. This might be the reason why modes 1 and 2 show a very high contribution (Figure 6a).

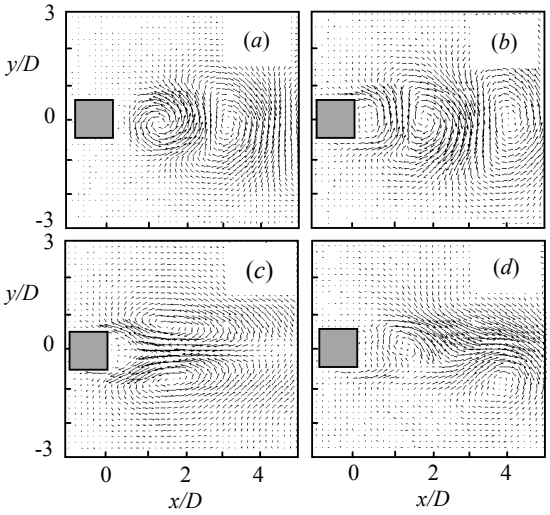

Figure 7: Spatial velocity fields for *SQ* using modes: (a) m = 1; (b) m = 2, (c) m = 3 and (d) m = 5

TWO-POINT CORRELATION FUNCTIONS

The two-point correlation functions are defined at a reference points (x_{ref}, z_{ref}) for the streamwise and spanwise fluctuating velocities at two locations separated in the streamwise and spanwise directions by Δx and Δz as follows: $R_{uu} = \langle u'(x_{ref}, z_{ref})u'(x_{ref} + \Delta x, z_{ref} + \Delta z)\rangle / \langle u_{rms}(x_{ref}, z_{ref})u_{rms}(x_{ref} + \Delta x, z_{ref} + \Delta z)\rangle$ and $R_{ww} = \langle w'(x_{ref}, z_{ref})w'(x_{ref} + \Delta x, z_{ref} + \Delta z)\rangle / \langle u_{rms}(x_{ref}, z_{ref})u_{rms}(x_{ref} + \Delta x, z_{ref} + \Delta z)\rangle$ where u' and w' are the streamwise and spanwise components of the velocity fluctuations at (x_{ref}, z_{ref}).

The contours of R_{uu} centred at downstream location, $x/D = 2.5$ with transverse and spanwise locations fixed, respectively at $y/D = 3.0$, and $z/D = 0$ for all the cylinder models are shown in Figure 8. The contours show that the cylinders with sharp upstream edges (SQ and DS) have relatively longer and larger spatial extents than those downstream of cylinders with more rounded upstream

edges (CC and DR). This implies that Tests SQ and DS generate stronger and larger organized motion. The corresponding R_{ww} contours (not shown) are much larger than those of R_{uu} in the spanwise direction plotted in Figure 8. The relatively smaller extent of R_{uu} compared to R_{ww} indicate that the spanwise velocity fluctuations would sustain strong correlation over a larger spanwise direction than the streamwise fluctuations.

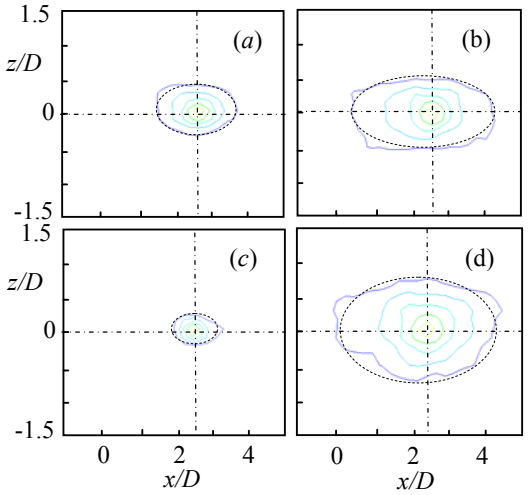

Figure 8: Contours of R_{uu} centred at x/D = 2.5: (a) CC, (b) SQ, (c) DR, and (d) DS. Note that outermost contours: R_{uu} = 0.5 with 0.1 spacing.

The two-point correlation profiles extracted from the streamwise and transverse slices through the centers of the contours shown in Figure 8 are, respectively, shown in Figures 9a and 9b. These profiles are used to quantitatively study the decay of the auto-correlations in the streamwise and spanwise directions. It is noted that $R_{uu}(z)$ decays more rapidly than the corresponding $R_{uu}(x)$ for each model. In addition, the decay is less rapid with Tests SQ and DS compared to Tests CC and DR.

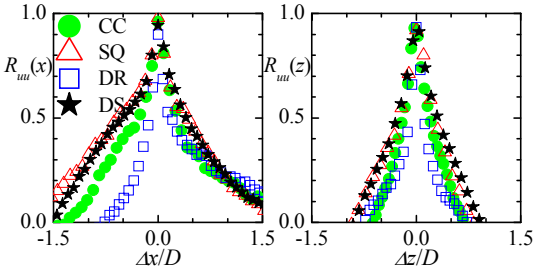

Figure 9: One-dimensional two-point correlation profiles extracted along the vertical and horizontal dash lines in Figure 8: (a) $R_{uu}(x)$ and (b) $R_{uu}(z)$.

Following previous studies (Volino *et al.*, 2007), the streamwise extent of R_{uu} (i.e., Lx_{uu}) and transverse extent R_{uu} (i.e., Ly_{uu}) were estimated. For example, the ratio Lx_{uu}/Ly_{uu} for CC and SQ are, respectively, 1.4 and 1.8. This also confirms the earlier assertion that cylinders with sharp upstream edges have relatively longer and larger spatial extents compared to cylinder with rounded upstream edges.

CONCLUSION

The effects of cylinders cross-section on evolution of turbulent wakes in circular, square, and trapezoidal-shaped has been investigated using PIV, POD, and two-point correlation functions. It was found that the flow characteristics depend strongly on the cross-section of the cylinder leading edge. The dominance of the first two POD modes and progression towards small scales structures with increasing mode is observed. In addition, the sharp upstream edges cylinders generate stronger and larger organized motion than cylinders with more rounded upstream edges.

ACKNOWLEDGEMENTS

The authors acknowledge the financial support provided by *CFI* and *NSERC* Discovery Grant.

REFERENCES

Adaramola, M.S., Sumner, D., and Bergstrom, D. J., 2007, "Turbulent Wake and Vortex Shedding for a Stack Partially Immersed in a Turbulent Boundary Layer," *Journal of Fluid Structures*, Vol. 23, pp. 1189–1206.

Coleman, H.W. and W.G. Steele, 1995, "Engineering Application of Experimental Uncertainty Analysis," *AIAA Journal,* Vol. 33, 1888-1896.

Forliti, D. J., Strykowski, P. J. and Debatin, K., 2000, Bias and Precision Errors of Digital Particle Image Velocimetry, *Experiments in Fluids*, Vol. 28(5), pp. 436 - 447.

Park, C. W., and Lee S. J., 2002, "Flow Structure around a Finite Circular Cylinder Embedded in Various Atmospheric Boundary Layers," *Fluid Dynamics Research* Vol. 30, pp. 197–215.

Park, C. W., and Lee S. J., 2004, "Effects of Free-end Corner Shape on Flow Structure around a Finite Cylinder," *Journal of Fluids and Structures* Vol. 19, pp.141–158.

Meyer, E. K., Pedersen, J. M., and Özcan, O., 2007, A Turbulent Jet in Cross-Flow Analyzed with Proper Orthogonal Decomposition, *Journal of Fluid Mech*anics, Vol.583, pp. 199-227.

Nakagawa, S., Nitta, K. and Senda, M., 1999, "An Experimental Study on Unsteady Turbulent near Wake of a Rectangular Cylinder in a Channel Flow". *Experiments in Fluids* Vol. 27 (3), 284 – 294.

Okamoto, K and Sunabashiri, Y., 1992, "Vortex Shedding from a Circular Cylinder of Finite Length Placed on a Ground Plane," *JSME International Journal Series* II, Vol. 114, pp. 512-521.

Ozgoren, M., 2006, "Flow Structure in the Downstream of Square and Circular Cylinders, *Flow Measurement and Instrumentation*, Vol. 17, pp. 225-235.

Prasad, A. K., Adrian, R. J., Landreth, C.C.,and Offutt, P.W., 1992, "Effect of Resolution on the Speed and Accuracy of Particle Image Velocimetry Interrogation," *Experiment in Fluids*, Vol. l3, pp. 105-116.

Raffel, M., Willert, C.E., and Kompenhaus, J., 1998. "Particle Image Velocimetry: A Practical Guide". New York, Springer.

Rempfer, D. and Fasel, H., 1994, "Evolution of Three-Dimensional Coherent Structures in a Flat-Plate Boundary Layer, *Journal Fluid Mech*., Vol.260, pp. 633-

Sirovich, L., 1987, Turbulence and the Dynamics of Coherent Structures, Part 1: Coherent Structures, *Quarterly Journal of Applied Mathematics* Vol.45, (3), pp. 561 – 571.

Sumner, D., Heseltine, J.L., and Dansereau, O.J.P., 2004, "Wake Structure of a Finite Circular Cylinder of Small Aspect Ratio," *Experiments in Fluids*, Vol. 37, pp. 720–730.

Zdravkovich, M. M., 2003, "Flow around Circular Cylinders Vol.2: Appl.". Oxford Univ. Press, NY.